Hockaday, S.A.C., Q. G. Reynolds, F. Dinter and T.M. Harms (2017). "Solar Thermal Treatment of Manganese Ore Fines". SolarPACES 2017, Solar Power and Chemical Energy Systems, 26 – 29 September 2017, Santiago de Chile

Solar Thermal Treatment of Manganese Ores

Susanna A.C. Hockaday[1, a)], Quinn G. Reynolds[1)], Frank Dinter[2)] and Thomas Harms [3)]

[1]*MINTEK. Address: Private Bag X3015, Randburg 2191, South Africa,*
[2]*Solar Thermal Energy Research Group (STERG), Mechanical Engineering Building, Joubert Street, Stellenbosch 7600, South Africa*
[3]*Department of Mechanical and Mechatronic Engineering, University of Stellenbosch, Joubert Street, Stellenbosch 7600, South Africa*

[a)]Corresponding author: linah@mintek.co.za

Abstract. Solar thermal treatment of manganese ores can potentially lower energy costs and reduce greenhouse gas emissions. The solar thermal treatment of three manganese ores resulted in thermal decomposition and reduction of the ores. Empirical results compared to thermodynamic equilibrium models and numerical heat transfer models informs the next steps towards proving the concept. The study provides information regarding the bulk thermal conductivity of manganese ores as determined by optimization of the heat transfer model parameters. Changes observed in the mass of the solar treated samples confirm thermal decomposition and reduction of manganese and iron minerals.

INTRODUCTION

The treatment of manganese ores is a possible application of concentrated solar thermal heat in the minerals processing field [1]. Other than sizing of the ore, the only beneficiation process currently practiced by South African mines is the sintering of fines to produce a product suitable for ferro-manganese alloy production.

The sintering process is beneficial as it drives off any surface or chemically-bound water, decomposes the carbonates in the ore (calcination), and achieves reduction of manganese minerals to Mn_2O_3 [2] while simultaneously agglomerating the ore fines into larger particles with suitable compressive strength for charging to smelters. Manganese smelters are either blast furnaces or submerged arc electric furnaces. Smelters heat the ore with a reductant such as coke to produce a molten metal product and a molten slag as waste. In addition to sintering, the pre-reduction and pre-heating of manganese ores have attracted interest as ways to lower energy requirements in smelters [3]. In smelters, the exothermic reaction of manganese oxides with carbon monoxide reduces the energy requirement, but the endothermic decomposition of carbonates ($MgCO_3$, dolomite and $CaCO_3$) as well as the endothermic reaction of carbon dioxide (CO_2) with carbon (C) to produce carbon monoxide (CO) has the opposite effect, increasing the smelter energy requirement.

Research on different pre-treatment options to optimize the energy efficiency of manganese ferro-alloy production and minimize the use of fossil fuels and/or electricity is happening globally. The reduction of low grade manganese ores by biomass has been found to occur at lower temperatures than with coal [4] leading to lower energy requirements for the pre-reduction. The merits of traditional sinter production versus pellets has also received attention [5]. Pellets

require an additional comminution stage, but can be heated at lower temperatures than sinter. An alternative process for high-carbon ferro-manganese production through self-reducing pellets has been proposed [6]. Direct current smelters have also been investigated as an alternative to alternating current smelters [7]. Against this background, the solar treatment of manganese ore is investigated in order to determine its suitability for pre-heating, pre-reduction and sintering.

EXPERIMENTAL

Two ore samples from the Kalahari manganese fields (A & B) as well as a sample from the Postmasburg ferruginous manganese deposit (C) were sourced from a South African high carbon ferromanganese producer. The ore samples were fines (-6 mm size fraction) and unsuitable for feed to a submerged arc furnace. The ore samples were pelletized with and without bentonite binder to investigate the production of solar fired pellets. Pulverizing the ores, wetting them with water and spinning them on a disk created the pellets. The size of pellets produced was in the range -13 mm + 6 mm.

(a) (b)

FIGURE 1. The experimental set-up showing the concentrator (a) and the box containing the ore sample (b).

The University of Stellenbosch rooftop solar facilities in South Africa provided thermal heat for the experiments. The concentrator is a flat mirror solar dish with two-axis tracking as shown in Fig. 1 (a). A quartz window kept the weighted samples in place while allowing the solar radiation to reach the sample as shown in Fig. 1 (b). K-type thermocouples were placed at various locations to describe a triangular section of the box at three levels. Each batch was irradiated for a period of at least an hour, but no longer than 90 minutes. A data logger, Agilent Model 34972 A, captured the temperature data every 5 seconds. Once the samples were heated for the required time, the concentrator was moved out of focus and the sample container was allowed to cool before removal. Insolation data for the duration of each test was obtained from The Southern African Universities Radiometric Network (SAURAN) [8]. Treated ores and pellets were cooled and then weighed to determine mass loss. Grab samples were sent for mineralogy and bulk chemistry analysis.

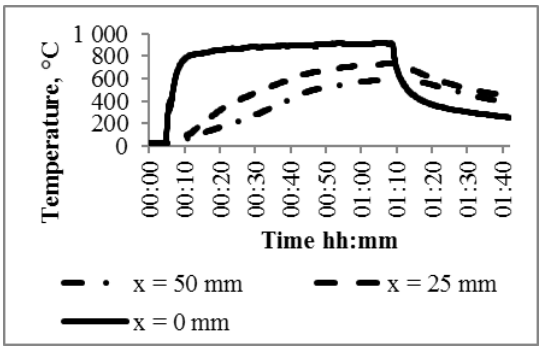

FIGURE 2. Recorded temperatures in center of sample box - experiment with ore B bonded pellets.

RESULTS AND DISCUSSIONS

Ten experiments were performed and used for heat transfer modelling. An example of the recorded temperatures may be seen in Fig. 2. The temperature at the quartz window rises quickly and is fairly constant after 30 min. Temperature increases through the samples were much slower and the temperature differential over the samples were between 350 °C and 560 °C at the conclusion of the experiments, indicating that thermal equilibrium was not reached. As the experiments progress, the increasing

temperature of the quartz window leads to increasing radiation losses - lowering the efficiency of the experimental set-up. Once the sample is removed from the focus, the quartz window cools down quickly, while the sample inside retains its heat much longer.

Description of Heat Transfer Modelling and Data Fitting Procedure

It is of interest for equipment design and scale-up purposes to determine an effective thermal conductivity for the static bed of particulate material tested during the solar experiments. Such an approach does not consider the contributions of additional energy transfer mechanisms and sources in the bed such as gas convection and chemical reaction; however, as a crude estimate it indicates any gross differences between ore types and particle dimensions.

The assumptions made for the present model include:

- Approximation of the bed as a continuum slab of material with constant and uniform thermal conductivity, effective density, and heat capacity.
- Approximation of the heat transfer mechanism in the bed as one-dimensional (perpendicular to hot face) and transient
- A single "concentration factor" η expressing the concentration ratio between the measured instantaneous direct normal insolation (DNI) and the energy flux experienced at the bed hot face
- A boundary condition at the hot face expressed in terms of a convective heat transfer coefficient and a surface emissivity, both pre-specified constants

Given that the bed is well insulated on all sides except for the insolation window at the hot face, the assumption of one-dimensional heat transfer into a semi-infinite slab seem justified. The transfer factor assumption is expected to be valid for a particular solar concentrator geometry with repeatable tracking behavior. The assumption of constant parameters in the heat transfer mechanism at the hot face is well-founded on classical heat transfer theory, with representative values determined from accepted empirical correlations [9]. With these assumptions, heat transfer through the bed in the solar sinter test equipment may be expressed simply as:

$$\frac{\partial T}{\partial t} = \frac{k_{eff}}{\rho C_p}\frac{\partial^2 T}{\partial x^2} \tag{1}$$

Here, $T(x,t)$ is the temperature at position x and time t, k_{eff} is the effective thermal conductivity of the bed material, ρ is its effective density, and C_P is its specific heat capacity. Equation (1) is subject to the following initial and boundary conditions:

$$T\big|_{t=0} = T_0 \tag{2}$$

$$-k_{eff}\left.\frac{\partial T}{\partial x}\right|_{x=0} = \eta q_0(t) - h(T - T_A) - \varepsilon\sigma(T^4 - T_A^4) \tag{3}$$

$$\left.\frac{\partial T}{\partial x}\right|_{x=\delta} = 0 \tag{4}$$

In these expressions, T_0 is the initial temperature of the bed at the start of the test, q_0 is the (time-dependent) solar insolation rate in W/m^2, T_A is the ambient temperature, h is the convective heat transfer coefficient between the hot face and ambient conditions, ε is the emissivity of the hot face surface (in this case quartz glass), σ is the Stefan-Boltzmann constant, and δ is the thickness of the bed from front to back. $x = 0$ is assumed to be the position of the hot face.

Although analytical closed and series solutions for equations (1)-(4) may be obtained if the boundary conditions are simplified further, a numerical solution approach based on the finite volume method [10] was chosen instead; this solves for the temperature profile through the slab at discrete intervals of t and x. The numerical approach was used primarily because it was desirable to include arbitrary time-dependent driving data such as solar insolation in the model, and it may also be of interest at a later stage to extend the heat transfer physics to include additional effects such as convection and chemical reaction – a numerical framework makes such extensions easier to implement. On modern computers, the performance difference between analytical and numerical calculation of solutions to equation (1) is negligible and there is minimal disadvantage in adopting a numerical approach.

The model and associated parameter fitting were implemented in the Python 3 programming language [11] on a machine running the Ubuntu 16.04 LTS Linux operating system. The NumPy 1.11.1 and SciPy 0.17.0 extension modules were used to provide matrix operations and generalized numerical least squares fitting functionality respectively. For all fitting calculations, the set of fixed parameters used is shown in Table 1.

TABLE 1. Fixed parameters used for all model fitting runs

Parameter	Value	Parameter	Value
δ	0.05 m	ρC_P	1 x 10^6 (J/m^3·K)
h	7.5 W/(m^2·K)	x resolution	100
ε	0.5	t resolution	100
T_A	298 K	T_0	(from test data)

In overview the algorithm involves reading of experimental data for a particular test, running multiple iterations of the numerical model in order to find a best fit for variables k_{eff} and η for that test, and reporting the results. Additional detail is shown in the flowsheets in Fig. 3 and 4.

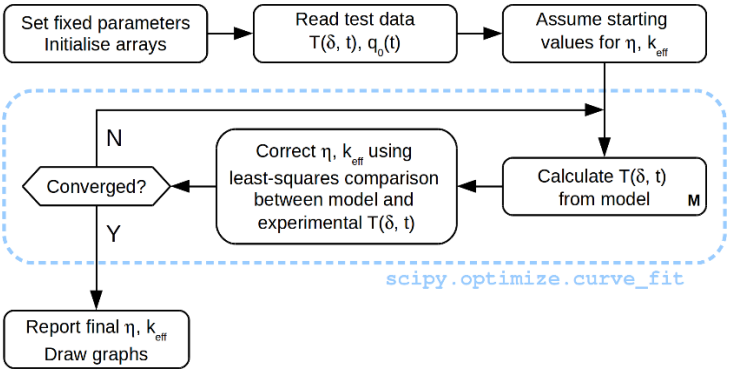

FIGURE 3. Flowsheet of algorithm to fit η and k_{eff} using model and experimental data

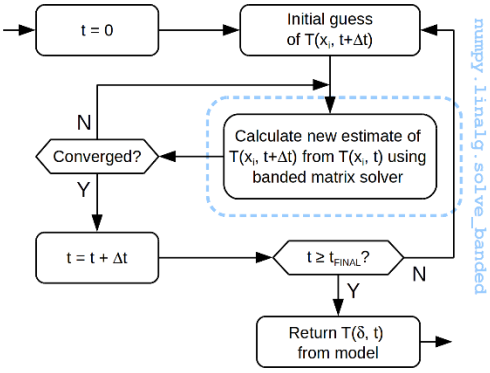

FIGURE 4. Flowsheet detail of block marked "M" in Fig. 3

In order to generate the results shown later in the paper, two sets of fitting calculations were run on the experimental data from all tests. In the first set, both η and k_{eff} were fitted to optimal values for each set of test data. However, since η is expected to be a constant for a particular piece of equipment, a second set of fitting calculations was then conducted by fixing the value of η for all tests at the average of that obtained from the first fits, and fitting only k_{eff}. Results from both fitting exercises are presented for solar tests on ore B fines and pellets in Fig. 5. The temperature modelled was positioned at the back of the test sample, 50 mm from the quartz window. Differences in the empirical and modelled temperatures are mainly due to the model assumptions neglecting chemical reactions and the discrete particulate nature of the samples. Both exothermic and endothermic reactions take place, which explain some of the deviations between the model and the experimental data.

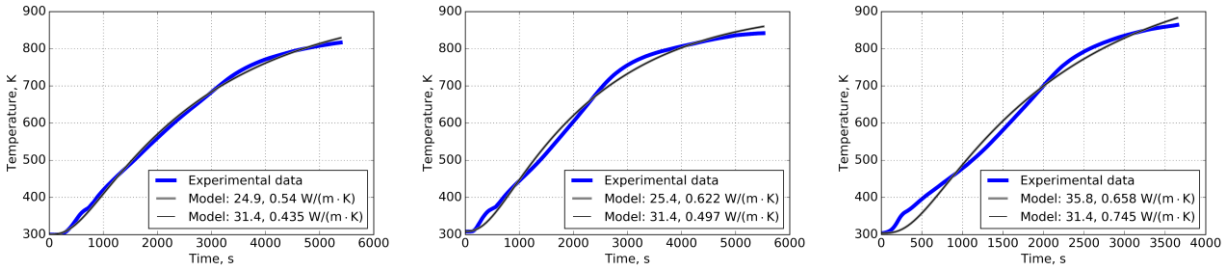

(a) (b) (c)

FIGURE 5. Results of heat transfer modelling of tests with ore B fines (a), pellets without binder (b) and pellets with binder (c)

From Fig. 6 it can be seen that effective conductivities for the ores were in the range of 0.51 to 0.54 W/(m·K). Effective conductivities for pellets ranged from 0.48 to 0.90 W/(m·K) and the experiment with 10 % coke mixed with pellets showed the highest effective conductivity at 1.3 W/(m·K). Pelletized samples showed improved heat transfer when compared to untreated ore fines. Improved heat transfer was also observed in pellets formed with binder (+) compared to pellets formed without binder. The experiment with ore A pellets with binder was repeated and the fitted effective conductivities differ by only 0.1 W/(m·K). The experiment with 10 % coke addition achieved the highest fitted value of 1.3 W/(m·K) indicating that coke addition improves heat transfer in the bulk sample. The fitted values for bulk thermal conductivities are much lower than values obtained for pure manganese ore disks [12], as these disks contained no air. Air in the test sample acts as an insulator and lowers the effective conductivity of the bed.

The concentration factors fitted for the experiments are shown in Fig. 7. By comparing the mirror area normal to insolation (2.563 m^2) with the focus area estimated as 150 mm x 150 mm (0.0225 m^2), a maximum concentration factor of 114 can be expected from the concentrator. The effective concentration factor determined by fitting the heat transfer model ranges from 24 to 45. The variation in the concentration factor is most likely due to factors such as dust build-up on the mirrors and variable convection losses not accounted for by the model. Other reasons for the lower effective concentration factor include mirror defects and shading by the receiver/sample container. The model will be extended in future to account for variation in convection losses. Dust build-up influenced concentrator efficiency and the highest efficiencies were obtained directly after cleaning of the mirrors during the tests with ore C pellets and ore A pellets.

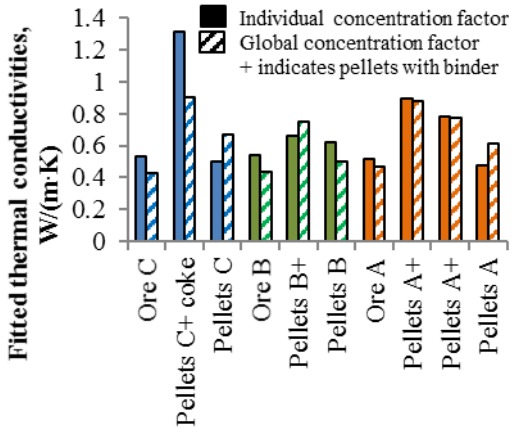

FIGURE 6. Fitted thermal conductivities for each experiment

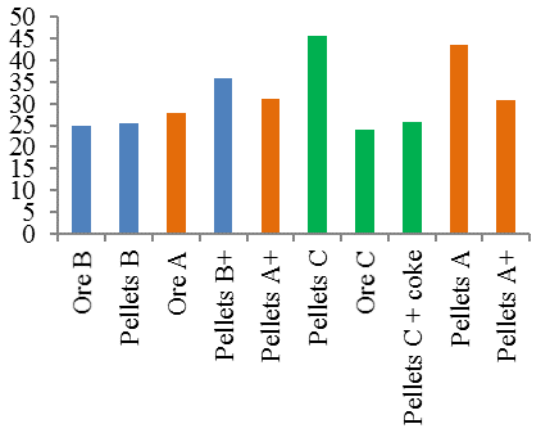

FIGURE 7. Effective concentration factors fitted for each experiment

Description of Thermodynamic Model

Results from the bulk chemical analysis and mineralogy of the ores were used to inform equilibrium models using FactSage 7.0 thermodynamic software [13]. The software uses minimization of the Gibbs free energy to determine the equilibrium of phases at different temperatures and has previously been found to predict the trends of manganese ores during reduction [14] and smelting [15] accurately. Since the thermodynamic database does not include data on all the mineralogical compounds in manganese ores, the ores were approximated by simplifying the mineralogy as shown in Table 2. Where possible, the simplified model conserved the valences of manganese and iron.

TABLE 2. Equilibrium model approximation of untreated ore mineralogy in mass%

Mineral	Ideal chemical formula	A*	A#	B*	B#	C*	C#
Hematite	Fe_2O_3	3.9	2.9	3.7	6.4	43.3	42.8
Hausmannite	Mn_3O_4	7.1		7.7			
Braunite	Mn_7SiO_{12}	38.1	43.2	33.8	49.1	13.6	21.7
Ankerite	$Ca(Fe,Mg,Mn)(CO_3)_2$	23.5	12.4	6.9	6.6		
Quartz	SiO_2	3.6	1.7	3.9	2	11.6	4
Calcite	$CaCO_3$	12.7	16.9	22.1	25.9	2.7	2.8
Rhodochrosite	$MnCO_3$		13.6				
Kuthnahorite	$Ca(Mn,Mg,Fe)(CO_3)_2$	6.5		7.8		1.6	
Cryptomelane	$KMn_6Mn_2O_{16}$			10		7.7	
Pyrolusite	MnO_2				6.4	5.9	14
Andradite	$Ca_3Fe_2Si_3O_{12}$		9.2				
$KAlSi_3O_8$	$KAlSi_3O_8$						4.3
	Other	4.6	0.1	4.1	3.6	13.6	10.4

* indicates bulk mineralogical assays by X-ray diffraction; # indicates composition for equilibrium model

The thermodynamic equilibrium models were used to determine the energy requirements and the composition changes with increased temperature for each ore sample based on Gibbs free energy minimization. Equilibrium models neglect kinetic effects – provided that reactions are not limited by kinetics, then experimental results will approach the predicted equilibrium. The mass loss of the sample is used as an indication of the extent of thermal decomposition and reduction reactions. Figures 8 to 10 compare the observed mass loss with the predicted mass loss of a sample at thermodynamic equilibrium.

Fig. 8 shows that ore A experiments did not achieve thermodynamic equilibrium. The three temperatures indicated for each experiment were obtained from thermocouples located in the center of the sample at 0 mm, 25 mm and 50 mm from the quartz window. The mass loss for the ore experiment is much lower than for the pellet experiments. Even though the hot face temperatures for the three pellet experiments were similar, two samples had approximately 8% mass loss and one sample had 10% mass loss. The higher temperatures achieved 25 mm from the quartz window, i.e. 719 °C for the higher mass loss experiment and 579 °C and 630 °C for the lower mass loss experiments explains these results, confirming the relationship between temperature and mass loss predicted by the thermodynamic model.

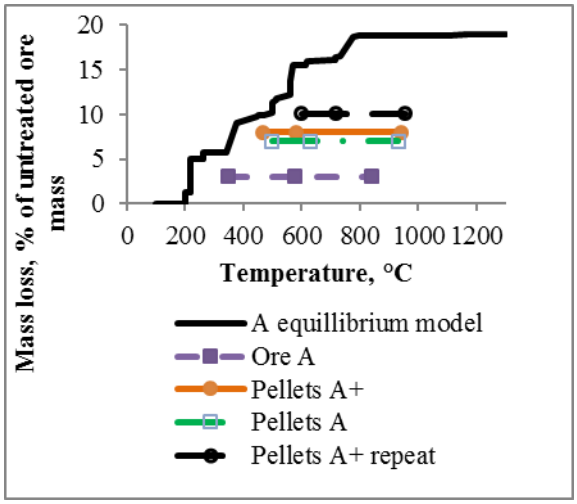

FIGURE 8. Comparison of empirical results with equilibrium model for ore A

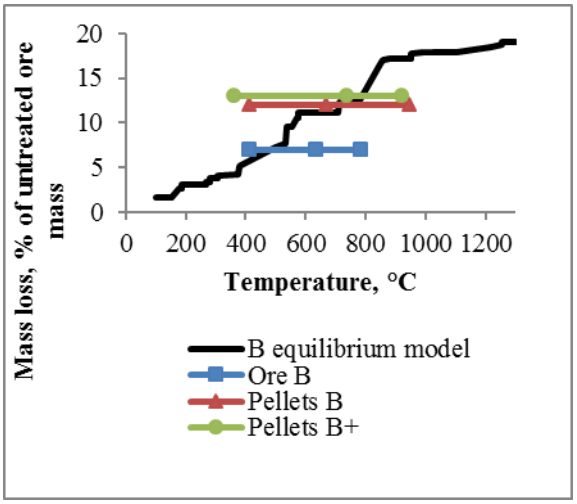

FIGURE 9. Comparison of empirical results with equilibrium model for ore B

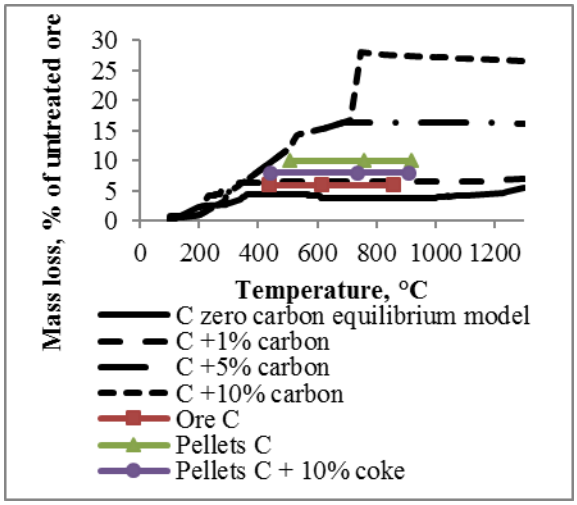

FIGURE 10. Comparison of empirical results with equilibrium model for ore C

The empirical results for ore B, given in Fig.9, show mass loss much closer to the equilibrium model prediction than for ore A. This suggests that ore B has faster reaction kinetics than ore A.

The mass loss observed empirically for experiments with ore C, shown in Fig. 10, exceeded the mass loss predicted by the equilibrium model for ore C alone, which would be thermodynamically impossible. However, during characterization of ore C organic material in the form of grassy roots and leaves were noticed. The organic material observed in the ore acts as a reductant and this leads to additional mass loss. The equilibrium model for ore C was adjusted to include a reductant, by adding between 1 % and 5 % of carbon to the ore. The model predicts that excess carbon and temperatures above 750 °C will lead to a sudden increase in mass loss as metallic iron is formed. This was not observed in the test with 10 % coke addition, indicating that the bulk of the sample did not reach temperatures above 750 °C.

CONCLUSIONS

A simple transient heat transfer model provided a good fit for experimental data and enabled the estimation of the bulk thermal conductivity of three manganese ores in air. This data is potentially of interest for engineering design and scale-up purposes. Improved heat transfer was observed for pellets compared to ore fines and for bonded pellets versus non-bonded pellets.

Although the solar test could not achieve sinter temperatures (1200 °C), the thermal decomposition and pre-heating of manganese ores with solar thermal energy has been conceptually proven by temperature measurements and mass losses achieved. Increased heat transfer will be needed to obtain higher temperatures throughout the samples. Further tests are planned using forced convection through the packed bed to improve the heat transfer between the hot face and the sample.

Higher energy inputs are required to achieve the temperatures needed for sintering of manganese ores and it is recommended that ways to increase the concentration factor of the experimental set-up should be investigated. Possible improvements could include using mirrors of higher quality, re-focusing the mirrors to eliminate any misalignment, adding additional mirrors and investigating a mirror coating to minimize dust build-up. The use of other solar concentrating facilities may also be considered.

ACKNOWLEDGMENTS

This paper is published by permission of Mintek. The authors would also like to thank Stellenbosch University and the Solar Thermal Energy Research Group (STERG) for the use of their concentrator and assistance in running the experiments, particularly JC Nel and Hein Joubert, SAURAN for direct normal insolation (DNI) data, and Transalloys Pty. Ltd. for donating the manganese ore samples for testing.

REFERENCES

1. Lina Hockaday, Frank Dinter and Thomas Harms. Opportunities for concentrated solar process heat in the minerals processing industry. In *SASEC 2016 Programme and Proceedings*, http://www.sasec.org.za/ Accessed July 2017.
2. Sverre E. Olsen, Merete Tangstad and Tor Lindstad. *Production of Manganese Ferroalloys*. (Tapir academic press, Trondheim, 2007), pp. 28-30.
3. Merete Tangstad, Michel Sibony, Stein Wasbø and Ragnar Tronstad. Kinetics of the prereduction of manganese ores. In *Conference proceedings, Infacon IX (Quebec)*, 2001, pp. 202-207.
4. Honglei Zhang, Guocai Zhu, Hong Yan, Tiancheng Li and Yuna Zhao. The mechanism on biomass reduction of low-grade manganese dioxide ore. *Metallurgical and Materials Transactions B*, **44**(4), 2013, pp. 889–896.
5. Thomas Brynjulfsen and Merete Tangstad. Melting and reduction of manganese sinter and pellets. In *Conference proceedings, INFACON XIII (Almaty)*, 2013, pp. 137 -148.
6. R. S. Braga, C. Takano and M. B. Mourão. Prereduction of self-reducing pellets of manganese ore. *Ironmaking & Steelmaking*, **34**(4), 2007, pp. 279–284.
7. H. Lagendijk, B. Xakalashe, T. Ligege, P. Ntikang and K. Bisaka. Comparing manganese ferroalloy smelting in pilot-scale ac and dc submerged-arc furnaces. In *Conference proceedings, INFACON XII (Helsinki)*, 2010, pp. 497 – 508.
8. M.J. Brooks, S. du Clou, J.L. van Niekerk, P. Gauche, C. Leonard, M.J. Mouzouris, A.J. Meyer, N. van der Westhuizen, E.E. van Dyk and F. Vorster. Sauran: A new resource for solar radiometric data in southern africa. *Journal of Energy in Southern Africa*, **26**, 2015, pp. 2–10.
9. J.R. Welty, C.E. Wicks and R.E. Wilson. *Fundamentals of Momentum, Heat, and Mass Transfer*. (Wiley & Sons, 1984) 3rd edition.
10. S.V. Patankar. *Numerical Heat Transfer and Fluid Flow*. (Hemisphere Publishing Corporation, 1980).
11. python™. https://www.python.org . Online, 2017. Accessed June 2017.
12. Michal Ksiazek. *The thermophysical properties of raw materials for ferromanganese production*. PhD thesis, Norwegian University of Science and Technology, 2012.
13. C.W. Bale, E. Bélisle, P. Chartrand, S.A. Decterov, G. Eriksson, K. Hack, I.-H. Jung, Y.-B. Kang, J. Melançon, A.D. Pelton, C. Robelin and S. Petersen. FactSage thermochemical software and databases recent developments. *Calphad*, **33**(2), 2009, pp. 295–311.
14. Bjorn Sorensen, Sean Gaal, Eli Ringdalen, Merete Tangstad, Ring Kononov and Oleg Ostrovski. Phase compositions of manganese ores and their change in the process of calcination. *International Journal of Mineral Processing*, **94**, 2010, pp. 101-110.
15. Eli Ringdalen, Sean Gaal, Merete Tangstad and Oleg Ostrovski. Ore melting and reduction in silicomanganese production. *Metallurgical and Materials Transactions B*, **41**, 2010, pp. 1220-1229.